A Supervisory Power Management System for a Hybrid Microgrid With HESS

Srikanth Kotra, *Student Member, IEEE*, and Mahesh Kumar Mishra, *Senior Member, IEEE*

***Abstract*—This paper proposes a supervisory power management system (PMS) for a grid interactive microgrid with a hybrid energy storage system. The key feature of the proposed PMS is reduced number of sensors required to implement the PMS. The PMS considers renewable power variation, grid availability, electricity pricing, and changes in local loads. It can detect the operating mode of system without measuring load currents and powers. A single-phase voltage source converter (VSC) transfers real power between dc grid and utility grid besides offering ancillary services such as harmonic mitigation, reactive power support, and unity power factor at the point of common coupling (PCC). In the proposed system, a better dc-link voltage regulation is achieved and the usage of supercapacitors reduces the current stress on the battery. The PMS also addresses extreme operating conditions such as load shedding, off-maximum power point tracking operation of photovoltaic, elimination of critical oscillation of hybrid energy storage systems power, islanded operation, and resynchronization with grid. The performance of the proposed PMS is verified by digital simulation and experimental studies.**

***Index Terms*—Battery, electricity pricing, hybrid energy storage system, photovoltaic (PV) power, power management, supercapacitor.**

I. Introduction

THE ever increasing demand for energy efficient appliances is promoting the use of dc appliances in residential and commercial sectors. DC appliances like LED lighting and inverter driven appliances like refrigerators, air conditioners are gaining popularity. At the same time, renewable energy based distribution system is encouraging the use of dc appliances to minimize conversion losses [1]. Therefore, both ac and dc loads will coexist in renewable-grid integrated distribution system [2]. However, the interconnection of renewable energy sources with grid is a concern for grid operators. When renewable energy sources (RESs) contribute a significant portion of power generation, their irregular and stochastic output variations can bring uncertainties in power system planning and operation. It is reported that many developed countries will supply 78% of their total power consumption using RES [3] by 2050. For example, South Korea plans to produce 12.5% of overall power generation by renewable by 2022. Out of that, 81% is supposed to be generated by the photovoltaic (PV) systems [4]. Therefore, the renewable power generation technology, which consists of PV and storage systems is required to ensure controllability, reliability, and stability of overall system.

Generally, hybrid energy storage systems (HESS) like battery and supercapacitor are employed in microgrids to improve reliability and life cycle. The high power density of supercapacitor increases the life cycle of battery [5]–[7]. In a microgrid with HESS, meeting the load demand by maintaining battery and supercapacitor SoCs within limits is an important task due to the uncertainties in RES power. Therefore, the power management system (PMS) plays a vital role in reliable and continuous operation of the microgrid.

In [8], an EMS is proposed which injects/draws power from grid according to the RES and load power changes. In this paper, it is assumed that the microgrid is always connected to the utility grid. Also, the supercapacitor doesn't absorb the transients when the battery reference current is set to zero, which increases the rate of change of battery current. This is due to the fact that the EMS changes the battery reference current instantly from zero to reference value during battery mode changes, i.e., idle to charging mode/discharging mode and vice versa. As a result, the battery is forced to respond quickly in spite of having supercapacitor units in the system.

A two-stage power control strategy is proposed in [9] to smoothen the power output of a grid-connected PV power plant. This technique is purely based on the difference between PV power and grid power. In [4], a unique energy management system is proposed for a grid interactive residential microgrid with energy storage. This method takes the dynamic pricing of grid power into account but does not consider the islanded operation of microgrid, which is frequent in residential power sector. In [10], a power balancing technique is proposed, which gives better dc-link regulation compared to [11]. However, the disturbances in the dc link have to be absorbed by battery, which increases the stress on it and thereby decreases the life of battery [12].

In [13]–[15], an integrated control and protection system is proposed for a microgrid. In these systems, the battery voltage rating should be equal to the dc-link voltage and any disturbance in RES and load should be buffered with battery units. Hence, battery experiences high current stress, which reduces it's

Manuscript received October 20, 2015; revised March 6, 2016, May 31, 2016, and August 1, 2016; accepted August 16, 2016. Date of publication January 16, 2017; date of current version April 10, 2017. This work was supported by the Ministry of Science and Technology, Department of Science and Technology, New Delhi, India, under the Project Grant SB/S3/EECE/056/2015.

The authors are with the Department of Electrical Engineering, Indian Institute of Technology Madras, Chennai 600 036, India (e-mail: ksrikanth225@gmail.com; mahesh@ee.iitm.ac.in).

Color versions of one or more of the figures in this paper are available online at http://ieeexplore.ieee.org.

Digital Object Identifier 10.1109/TIE.2017.2652345

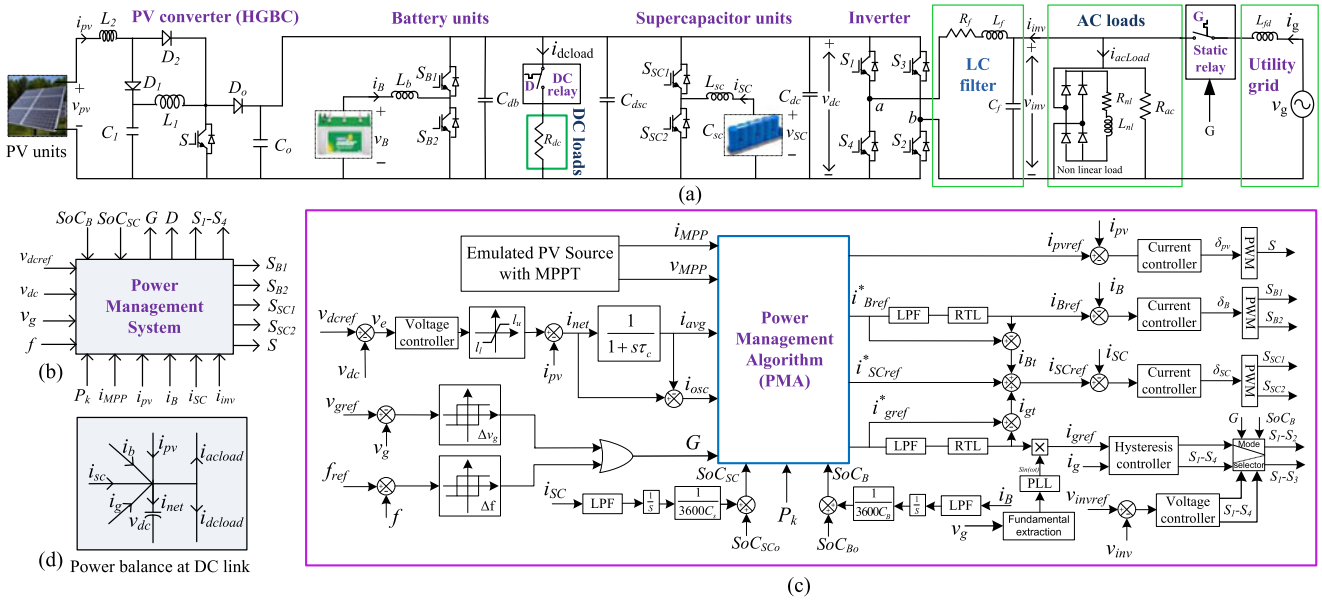

Fig. 1. System configuration and proposed PMS. (a) Configuration of grid interactive microgrid with HESS. (b) Block diagram of PMS. (c) Proposed PMS. (d) Power balance at dc link.

lifespan [5]. Also, this method is based on difference between load power and source powers. In [16], a power management method is developed for distributed generators (DG) operating under a common feeder. This method employs communication line to each DG for islanding and grid connection. However, the individual DGs are controlled by measuring difference between source power and load power. In [17], a state machine approach based power management is proposed, which gives better performance compared to [18]. This method uses fuzzy controller to maintain desired SoC of battery banks and considers 15 distinct operating modes of the microgrid. However, the off-MPPT mode is not covered in any of the 15 modes. Also, the fixed SoC limits are used in this work.

A rule-based control scheme is proposed in [19] to dispatch intermittent renewable energy sources using a BESS. The objective of this control scheme is to maintain the battery SoC within limits while supplying the power difference. However, this scheme does not discuss power balancing when the battery is fully charged/discharged. Also, the dc-link voltage regulation is not demonstrated and the local loads are not considered in the system. In [20], a deterministic EMS is proposed for a grid interactive microgrid. This system employs a microturbine to support loads in deficit power mode. This system employs communication from each microgrid to the central controller and forecasting of load, PV powers to generate reference quantities. However, it requires measurement of load currents to calculate powers, which increases the computation.

A power control strategy is devised in [21] to balance power in a dc microgrid using a battery bank. The main focus of this paper is to develop a dedicated local control system to maintain battery SoC and provide an over charge security. The literature in [22]–[25] describes the control strategies for a microgrid, which operate the system based on dc-link voltage variation. However, the variable dc-link voltage affects the performance of dc loads. In [26], a model predictive control based power management scheme is proposed for a dc microgrid using HESS, which gives a uniform discrete design approach. However, the dc-link voltage is assumed to be constant.

According to these research works, the first step in designing an EMS is to identify operating mode of the microgrid. In the literature, there are only two techniques available to identify the operating mode of the microgrid. One is based on power difference and the other is based on dc-link voltage variation. In this paper, we proposed a mode identification technique based on dc-link voltage controller output, which strictly regulates the dc-link voltage. Second, there is a need to develop a unified supervisory controller to address every operating mode of the system with minimal components. In this paper, we formulated a power management algorithm that addresses all possible operating modes of a microgrid and achieves stable and desirable performance in all modes with reduced number of sensors.

II. System Configuration and Proposed PMS

The grid interactive microgrid with HESS considered in this paper is shown in Fig. 1(a). The emulated PV source is connected to the common dc link through a high gain boost converter (HGBC) and a single-phase inverter is interfacing dc link and utility grid, as shown in Fig. 1(a). The battery and supercapacitor units are interfaced with the common dc link through a bidirectional buck-boost converter each, as shown in Fig. 1(a). The battery unit supplies/handles average deficit/excess power and the supercapacitor unit supplies or absorbs power surges.

The proposed PMS, shown in Fig. 1(b), mainly consists of dc-link voltage controller, reference current generation from power management algorithm (PMA), battery and grid current

smoothing, islanding and resynchronization detection, and converter control scheme, as shown in Fig. 1(c).

A. DC-Link Voltage Controller

The power balance in the system is achieved by maintaining constant dc-link voltage, as shown in Fig. 1(d). The voltage control loop generates the reference current (i_{net}) to be injected/drawn into/from the dc link to maintain reference voltage at the dc link, as shown in Fig. 1(c)

$$v_e(t) = v_{\text{dcref}}(t) - v_{\text{dc}}(t)$$
$$i_{\text{net}}(t) = k_{p1} v_e(t) + k_{i1} \int v_e(t)dt - i_{\text{pv}}(t) \quad (1)$$

where k_{p1} and k_{i1} are PI controller gains. It is to be noticed that i_{net} is positive when v_e is positive, which implies that the dc-link input power is more than the output power and vice versa. This nature of i_{net} can be utilized to identify the operating mode of the microgrid. The power balance in the system is

$$p_l(t) + p_{\text{loss}}(t) - p_{\text{pv}}(t) = p_{\text{net}}(t) \quad (2)$$

where $p_l(t)$ is the sum of ac and dc load powers, i.e., $p_l(t) = p_{\text{dcload}} + p_{\text{acload}}$. The terms $p_{\text{pv}}(t)$ and $p_{\text{loss}}(t)$ refer to PV power and power loss in the system and $p_{\text{net}}(t)$ is the net power required to regulate the dc-link voltage. Here, $p_{\text{net}}(t)$ should be supplied by battery or grid along with supercapacitor.

The controller output $i_{\text{net}}(t)$ is derived from the dc-link voltage control loop, as shown in Fig. 1(a), and is given by (1). The average component, i.e., $i_{\text{avg}}(t)$ is extracted by using a low-pass filter [24] as

$$i_{\text{avg}}(t) = \frac{1}{1 + s\tau_c} i_{\text{net}}(t) \quad (3)$$

where $f_c = 1/\tau_c$ is the cutoff frequency of the low-pass filter. f_c is selected to be 5 Hz such that the battery/grid currents respond to changes with more than 0.2 s time period. The oscillating component of $i_{\text{net}}(t)$ is extracted as follows:

$$i_{\text{osc}}(t) = i_{\text{os}}(t) + i_{\text{tr}}(t) = \left(1 - \frac{1}{1 + s\tau_c}\right) i_{\text{net}}(t). \quad (4)$$

The PMA allocates $i_{\text{osc}}(t)$ to supercapacitor and $i_{\text{avg}}(t)$ to utility grid/battery/PV depending on $i_{\text{avg}}(t)$, availability of grid and status of battery SoC. Effectively, $i_{\text{avg}}(t)$ decides the operating mode of microgrid.

B. Power Management Algorithm

The PMA decides the operating mode of the system based on $i_{\text{avg}}(t)$, as shown in Fig. 2. The PMA is formulated with following operational objectives.

1) To identify the operating mode of the system and make decisions based on $i_{\text{avg}}(t)$.
2) To achieve power balance in every operating mode.
3) maintain Battery and supercapacitor SoCs within limits and to eliminate current oscillation of HESS at the verge of SoCs.

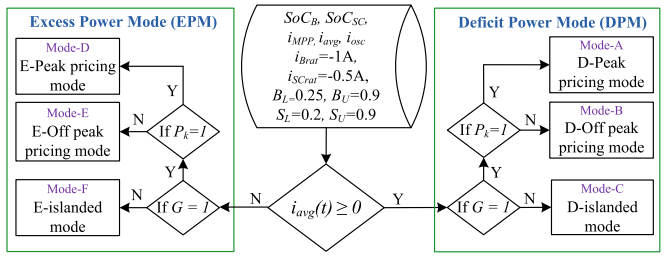

Fig. 2. Simplified block diagram of PMA.

4) supply average power by battery only if the system is islanded.
5) supply oscillating and transient peak powers by supercapacitor only.
6) minimize/maximize power drawn/supplied from/to grid during peak pricing.
7) provide minimum backup for critical loads in the islanded mode.

There are three possible operating modes of the system, namely, 1) deficit power mode (DPM), 2) floating power mode (FPM), and 3) excess power mode (EPM). FPM is merged with DPM as the HESS can be charged from grid in both modes. Hence, there are two effective operating modes, as shown in Fig. 2.

In both modes of operation, there are three submodes based on the availability of grid (G) and peak pricing status (P_k), as shown in Fig. 2. They are: 1) peak pricing mode, 2) off-peak pricing mode, and 3) islanded mode. In each submode, SoC_B and SoC_{SC} are monitored and maintained within limits. If grid power pricing is high, then P_k is set to high (1), else set to low (0). Similarly, when the system is connected to grid then G is set to high (1), else set to low (0). A rule-based control [27] is developed to implement the PMA. The algorithm is initialized with battery SoC lower limit B_L and upper limit B_U are set to 0.25 and 0.9, respectively, and supercapacitor SoC lower limit S_L and upper limit S_U are set to 0.2 and 0.9, respectively.

1) Deficit Power Mode: ($i_{\text{avg}} \geq 0$) *(Cases: 1–14):* In DPM, the average current ($i_{\text{avg}}(t)$) is greater than or equal to zero, and there are three submodes explained as following.

Mode A: *D-peak pricing mode (Cases: 1–4)*

In this mode, grid is ON and peak pricing is enabled, i.e., $G = 1, P_k = 1$. Therefore, minimum amount of power is drawn from the grid. The deficit power is drawn from grid while charging battery and supercapacitor upto 50% of their capacity by updating $B_L = 0.5$ and $S_L = 0.5$. There are four possible cases depending on SoC_B and SoC_{SC}, as shown in Fig. 3. In those four cases, battery and supercapacitor are charged if their SoCs are less than their respective lower limits, else battery will be idle and supercapacitor supplies transient and oscillating powers, as shown in Fig. 3.

Mode B: *D-off peak pricing mode (Cases: 5–8)*

In this mode, grid is ON and peak pricing is disabled, i.e., $G = 1, P_k = 0$. As the grid power pricing is less, the deficit power is drawn from grid while charging battery and supercapacitor upto

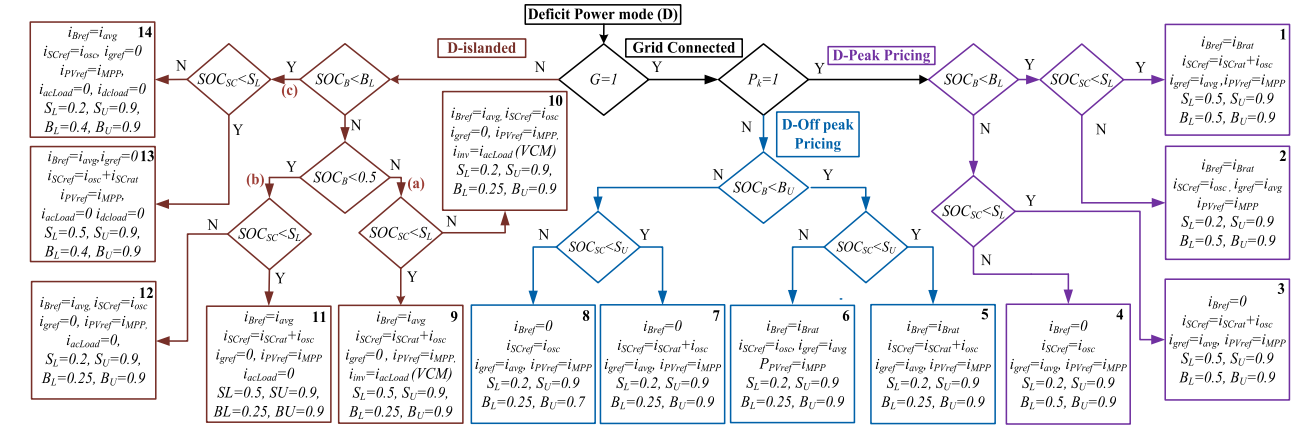

Fig. 3. Flowchart of deficit power mode.

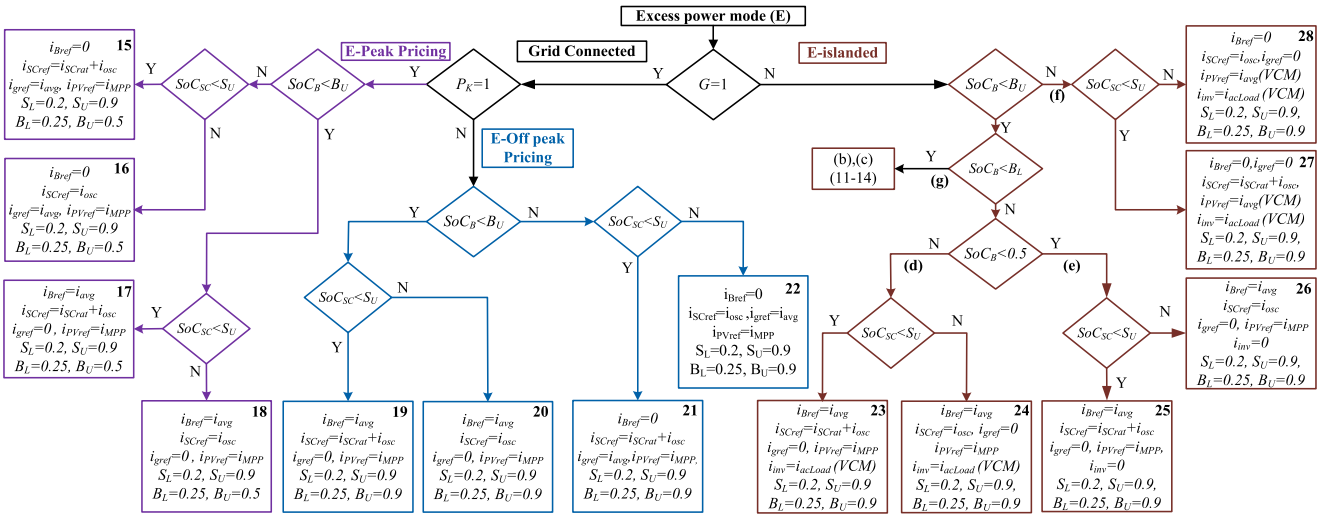

Fig. 4. Flowchart of excess power mode.

90% of their capacity by updating $B_U = 0.9$ and $S_U = 0.9$, as shown in Fig. 3.

Mode C: *D-islanded mode (Cases: 9–14)*

In this mode, grid is OFF, i.e., $G = 0$. Therefore, the deficit power is to be supplied by HESS or proportionate load should be shed. There are three branches (a), (b), and (c) in this mode, as shown in Fig. 3.

a) *Cases 9–10*: If SoC_B is more than 0.5, then both dc and ac loads are supplied power from battery and inverter is operated in voltage control mode (VCM) to supply power to ac loads at rated voltage and frequency. The supercapacitor supplies oscillating power while regulating its SoC.

b) *Cases 11–12*: If SoC_B is between B_L and 0.5, then dc loads are supplied and ac loads are turned OFF by resetting inverter pulses.

c) *Cases 13–14*: If SoC_B is less than B_L, then both ac and dc loads are turned OFF and the total power from PV is fed to the battery.

In Cases 11–14, the system may enter into excess power mode due to load shedding. Therefore, the same cases are readdressed in E-islanded mode, as shown in Fig. 4.

2) Excess Power Mode: ($i_{\text{avg}} < 0$) *(Cases: 15–28):* In EPM, the average current $i_{\text{avg}}(t)$ is less than zero and there are three submodes explained as following.

Mode D: *E-peak pricing mode (Cases: 15–18)*

In this mode, grid is ON and peak pricing is enabled, i.e., $G = 1, P_k = 1$. Therefore, maximum possible amount of excess power is injected into the grid by limiting battery and supercapacitor charging up to 50% of their capacity by updating $B_L = 0.5$ and $S_L = 0.5$. As the power is injected into the grid, it is referred as *grid injecting mode*.

Mode E: *E-off peak pricing mode (Cases: 19–22)*

In this mode, grid is ON and peak pricing is disabled, i.e., $G = 1, P_k = 0$. Therefore, the excess power is preferred to charge battery and supercapacitor upto 90% of their capacity by updating $B_U = 0.9$ and $S_U = 0.9$, as the pricing of power injected into the grid is less. Once the battery and supercapacitor are fully charged, the excess power is injected into grid.

Mode F: *E-islanded mode (Cases: 23–28)*

In this mode, grid is OFF, i.e., $G = 0$. Therefore, the excess power has to be absorbed by HESS or the PV power should be controlled such that it is equal to load power. There are four branches in this mode, as shown in Fig. 4.

d) *Cases 23–24*: In this mode, SoC_B is more than 0.5. Therefore, both ac and dc loads are supplied from PV and inverter is operated in VCM to maintain rated voltage and frequency on ac side. If any excess power is available, it is utilized to charge the battery and the supercapacitor.

e) *Cases 25–26*: In this mode, SoC_B is in between B_L and 0.5. Therefore, dc loads are supplied and ac loads are turned OFF and the excess power is used to charge battery.

f) *Cases 27–28*: In this mode, SoC_B is more than B_U. Therefore, PV is operated in *off-MPPT mode*. In other words, PV is operated in VCM.

g) *Cases 11–14*: If SoC_B is less than B_L, then deficit mode Cases 11–14 are executed until SoC_B increases beyond B_L.

C. Battery and Grid Current Smoothing

The battery and grid reference currents generated by PMA causes battery and grid to undergo current stress during mode changes. Therefore, to reduce the rate of change of battery current and to achieve a seamless mode transfer of grid from grid supply mode to grid injecting mode and grid-connected mode to islanded mode and vice versa, the sudden changes in $i_{\mathrm{Bref}}(t)$ and $i_{\mathrm{gref}}(t)$ are allocated to the supercapacitor as given by the following equation:

$$i_{\mathrm{SCref}}(t) = i_{\mathrm{osc}}(t) + i_{\mathrm{Bt}}(t) + i_{\mathrm{gt}}(t) \tag{5}$$

where $i_{\mathrm{SCref}}(t)$ is the supercapacitor reference current, $i_{\mathrm{osc}}(t)$ is the net sum of oscillating and transient currents and $i_{\mathrm{Bt}}(t)$, $i_{\mathrm{gt}}(t)$ are battery and grid transient currents, respectively.

D. Smooth Islanding and Resynchronization

In the proposed system, the microgrid islanding is detected by over/under voltage/frequency method [28]. The microgrid is islanded if the grid voltage deviates from 0.88–1.1 per unit or the frequency deviates from 49.3–50.5 Hz complying with the IEEE Standard 1547. When the microgrid is islanded, the grid status G is updated to 0 and the PMA sends a command signal to the grid relay and the inverter is operated in VCM. Once the grid voltage and frequency are restored, the relay is closed at zero crossing of grid voltage and the inverter is operated in current control mode (CCM). Accurate grid synchronization is achieved by generating grid current reference from grid voltage using the phase-locked loop (PLL). An indirect current control strategy is employed in this paper, which gives the feature of unity power factor and sinusoidal grid current [8].

III. Stability Analysis of Proposed Microgrid

The stability analysis of proposed system is done by considering 5 ms of communication delay for all converters. The power balance and stability in the system are monitored by regulating the dc-link voltage. The dc-link voltage controller remains same in all control strategies. The dc-link voltage controller is designed such that it provides the desired phase margin and gain margin with any of the three converters, i.e., battery or PV or grid converters after considering communication delays.

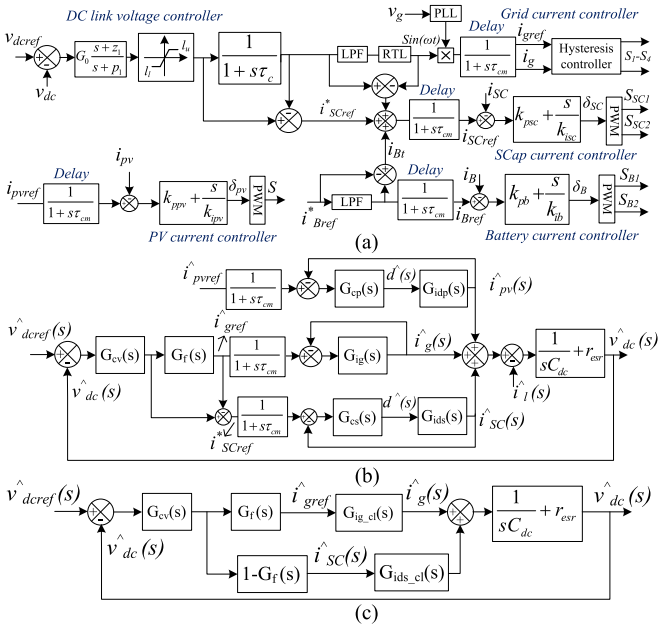

Fig. 5. Control block in grid-connected mode. (a) Control block diagram. (b) Small-signal model. (c) Simplified small-signal model.

There are mainly three control strategies in the proposed PMS. They are as follows.

1) grid-connected mode: Grid maintains v_{dc} in this mode.
2) Islanded mode: Battery maintains v_{dc} in this mode.
3) Off-MPPT mode: PV maintains v_{dc} in this mode.

The control block diagram in grid-connected mode is shown in Fig. 5(a) and the small-signal model is derived as shown in Fig. 5(b).

To derive the loop gain from reference voltage to output voltage, other disturbances are made zero and the simplified model shown in Fig. 5(c) is obtained. Where $G_{\mathrm{cv}}(s)$, $G_f(s)$, $G_{\mathrm{ig}}(s)$, $G_{\mathrm{cs}}(s)$, $G_{\mathrm{ids}}(s)$, $G_{\mathrm{cp}}(s)$, and $G_{\mathrm{idp}}(s)$ are transfer functions of dc-link voltage controller, low-pass filter, grid converter, supercapacitor current controller, supercapacitor converter in current control mode, PV current controller, and PV converter in current control mode, respectively.

The loop gain of the simplified small-signal model is

$$GH(s) = G_{\mathrm{cv}}(s)[G_f(s)G_{\mathrm{ig\_cl}}(s) + (1 - G_f(s))G_{\mathrm{idsc\_cl}}] \times \left[\frac{1}{sC_{\mathrm{dc\_total}}} + R_{\mathrm{esr}}\right] \tag{6}$$

where $G_{\mathrm{cv}}(s) = G_0\left(\frac{s+z_1}{s+p_1}\right)$, $G_f(s) = \frac{1}{1+s\tau}$

$$G_{\mathrm{cs}}(s) = k_{\mathrm{ps}} + \frac{k_{\mathrm{is}}}{s}G_{\mathrm{ids}}(s) = \frac{s(C_{\mathrm{dc\_total}}V_{\mathrm{dc}}) + 2D'I_{\mathrm{Lsc}}}{s^2L_{\mathrm{sc}}C_{\mathrm{dc\_total}} + s\frac{L_{\mathrm{sc}}}{R_L} + D'^2}$$

and $G_{\mathrm{idsc\_cl}}(s) = \frac{G_{\mathrm{cs}}(s)G_{\mathrm{ids}}(s)}{1+G_{\mathrm{cs}}(s)G_{\mathrm{ids}}(s)} * \frac{1}{1+s\tau_c}$ and $G_0 = 347.5542$, $z_1 = 0.06779$, $p_1 = 27.2018$, $\tau = 0.7$, $k_{\mathrm{pgi}} = 0.5$, $k_1 = 0.5$, $k_3 = 0.5$, $k_{\mathrm{ps}} = 0.4$, $k_{\mathrm{is}} = 0.1$, $L_{\mathrm{sc}} = 5$ mH, $R_L = 100\ \Omega$, $D' = 0.48$, $I_{\mathrm{Lsc}} = 5$ A, and $C_{\mathrm{dc_total}} = 2860\ \mu$F.

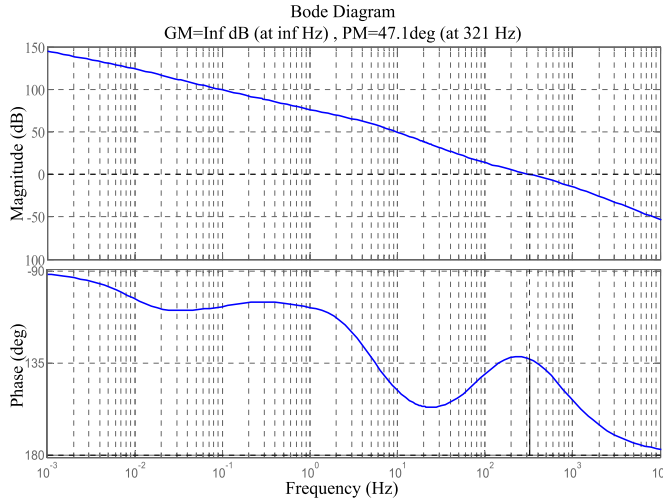

Fig. 6. Bode plot of control loop gain in grid-connected mode.

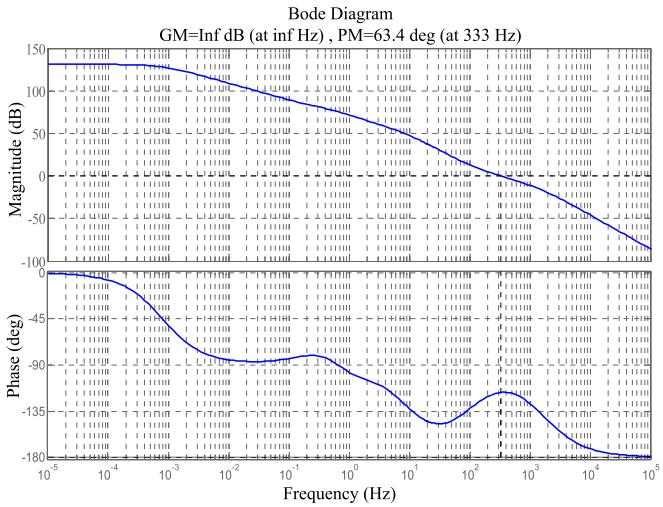

Fig. 8. Bode plot of control loop gain in islanded mode.

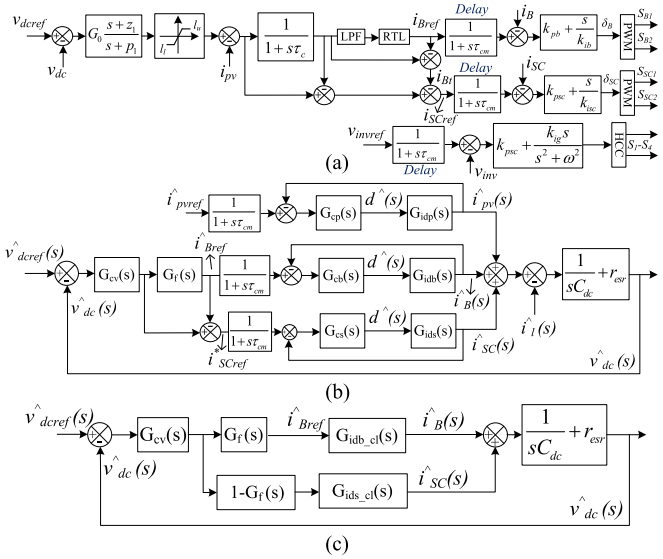

Fig. 7. Control block in islanded mode. (a) Control block diagram. (b) Small-signal model. (c) Simplified small-signal model.

With these design parameters the Bode plot of the system is shown in Fig. 6. It can be observed that the grid current control loop has infinity gain margin and a phase margin of 47.1° and dc bus voltage is stable for changes in grid reference current. This also implies that the dc bus voltage is stable when the system changes its mode form islanded to grid-connected.

Similarly, the control block diagram, small-signal model and simplified small-signal model for islanded mode are shown in Fig. 7. The loop gain of the control loop in islanded mode is given by

$$GH(s) = G_{cv}(s)[G_f(s)G_{idb\_cl}(s) + (1 - G_f(s))G_{ids\_cl}] \times \left[\frac{1}{sC_{dc\_total}} + R_{esr}\right] \quad (7)$$

where $G_{cb}(s) = k_{pb} + \frac{k_{ib}}{s}$, and $k_{pb} = 0.01$, $k_{ib} = 0.5$, $L_b = 5$ mH, $R_L = 100$, $D' = 0.6$, $I_{Lb} = 10$ A, $G_{idb\_cl}(s) = \frac{G_{cs}(s)G_{ids}(s)}{1+G_{cs}(s)G_{ids}(s)}$, and $G_{idb}(s) = \frac{s(C_{dc\_total}V_{dc})+2D'I_{Lb}}{s^2 L_b C_{dc\_total} + s\frac{L_b}{R_L} + D'^2}$.

The only change in loop gain of islanded mode to grid-connected mode is that the closed loop transfer function of grid converter is replaced by that of battery converter. With the above design parameters the Bode plot of the system is shown in Fig. 8. With battery converter, the phase margin is found to be 63.4°. It can be observed that the phase margin of loop gain with grid converter and battery converter is almost same due to the fact that the closed loop transfer function of the battery converter is unity till the cross over frequency, which does not affect the gain cross over frequency. Therefore, the system is stable in islanded mode. This also implies that the dc grid is stable when the system is islanded from utility grid. Similarly, the stability in Off-MPPT mode is verified.

IV. Simulation Results

The proposed system is modeled using MATLAB/Simulink tool and the efficacy of proposed PMS is verified in all modes of operation by changing grid availability, peak pricing, HESS SoCs, and maximum power point current of PV, as shown in Fig. 9(a)–(c). The simulation is carried out for a duration of 40 s to test all the 28 modes of operation, as explained in the following section and tabulated in Table II.

A. Deficit Power Mode (Cases: 1–14)

1) D-Peak Pricing Mode (Cases: 1–4): The system is started at t = 0 s with utility grid is ON state, peak pricing is enabled, i_{MPP} is set to 1 A and $SoC_B < B_L$ and $SoC_{SC} < S_L$. At t = 0 s, supercapacitor supplies peak current until the battery reaches steady state and dc-link voltage settles at rated value. In Case 1, i.e., 0–2 s, grid supplies average deficit power and battery, supercapacitor units are charged with rated currents 1 and 0.5 A, respectively, as their SoCs are less than the lower limits

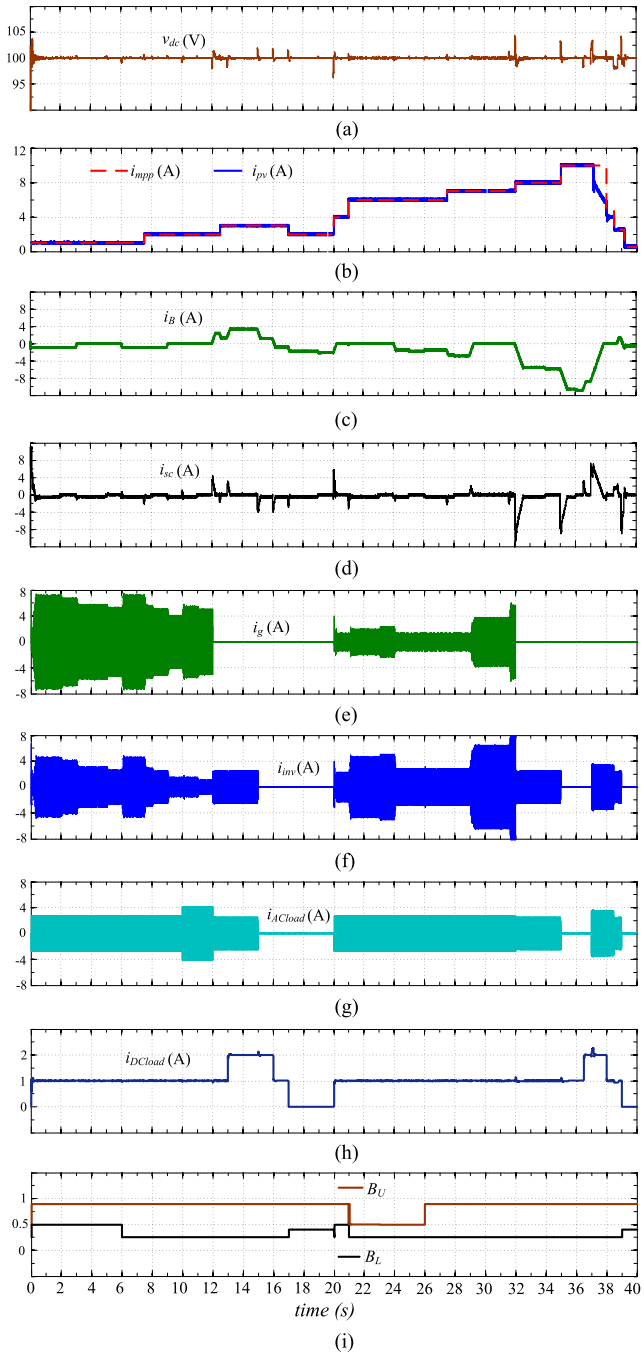

Fig. 9. Performance of microgrid with proposed PMS. (a) DC bus voltage. (b) MPPT reference current and PV current. (c) Battery current. (d) Supercapacitor current. (e) Grid current. (f) Inverter current. (g) AC load current. (h) DC load currents. (i) Battery upper and lower SoC limits.

TABLE I
SYSTEM PARAMETERS

Parameter	Values
Battery Pack: Ah Capacity, Terminal voltage	26 Ah, 60 V
Supercapacitor Pack: C, V_{rated}, I_{peak}	19.33 F, 48 V, 200 A
Battery converter: L_b, C_{db}	5 mH, 220 μF
Supercapacitor converter: L_{sc}, C_{dsc}	5 mH, 220 μF
HGBC parameters: L_1, L_2, C_0	5 mH, 5 mH, 220 μF
VSC Parameters: C_{dc}, C_f	2200 μF, 10 μF
L_f, R_f	10 mH, 0.1 Ω
AC and dc loads: R_{dc}, R_{ac}	100 Ω, 50 Ω,
R_{n1}, L_{n1}	50 Ω, 50 mH
Utility and dc-link voltage: V_g and V_{dc}	50 V and 100 V

TABLE II
OPERATING MODES OF THE SYSTEM

Cases	*Sim*	*Exp*	P_{pv}	*Grid*	P_k	SoC_B	SoC_{SC}	i_B	i_{SC}	i_{inv}	i_{pv}	B_L	B_U
Case 1	0--1	t_1-t_2	<P_L	*on*	1	0.2	0.15	i_{Brat}	$i_{SCrat}+i_{osc}$	*CCM*	i_{MPP}	0.5	0.9
	1--2	t_2-t_3	<P_L	*on*	1	0.4	0.4	i_{Brat}	$i_{SCrat}+i_{osc}$	*CCM*	i_{MPP}	0.5	0.9
Case 2	2--3	t_3-t_4	<P_L	*on*	1	0.4	0.6	i_{Brat}	i_{osc}	*CCM*	i_{MPP}	0.5	0.9
Case 3	3--4	t_6-t_7	<P_L	*on*	1	0.6	0.15	*0*	$i_{SCrat}+i_{osc}$	*CCM*	i_{MPP}	0.5	0.9
	4--5	t_6-t_7	<P_L	*on*	1	0.6	0.4	*0*	$i_{SCrat}+i_{osc}$	*CCM*	i_{MPP}	0.5	0.9
Case 4	5--6	t_4-t_5	<P_L	*on*	1	0.6	0.6	*0*	i_{osc}	*CCM*	i_{MPP}	0.5	0.9
Case 5	6--8	t_8-t_9	<P_L	*on*	0	0.7	0.7	i_{Brat}	$i_{SCrat}+i_{osc}$	*CCM*	i_{MPP}	0.25	0.9
Case 6	8--9	t_9-t_{10}	<P_L	*on*	0	0.7	0.95	i_{Brat}	i_{osc}	*CCM*	i_{MPP}	0.25	0.9
Case 7	9--11		<P_L	*on*	0	0.95	0.7	*0*	$i_{SCrat}+i_{osc}$	*CCM*	i_{MPP}	0.25	0.9
Case 8	11--12	t_1-t_8	<P_L	*on*	0	0.95	0.95	*0*	i_{osc}	*CCM*	i_{MPP}	0.25	0.9
Case 9	12--14	t_1-t_9	<P_L	*off*	0	0.7	0.15	i_{avg}	$i_{SCrat}+i_{osc}$	*VCM*	i_{MPP}	0.25	0.5
Case 10	14--15	t_{12}-t_{13}	<P_L	*off*	0	0.7	0.6	i_{avg}	i_{osc}	*VCM*	i_{MPP}	0.25	0.9
Case 11	15--16		<P_L	*off*	0	0.45	0.15	i_{avg}	$i_{SCrat}+i_{osc}$	*0*	i_{MPP}	0.25	0.9
Case 12	16--17	t_{13}-t_{14}	<P_L	*off*	0	0.45	0.6	i_{avg}	i_{osc}	*0*	i_{MPP}	0.25	0.9
Case 13	17--19		<P_L	*off*	0	0.2	0.15	i_{avg}	$i_{SCrat}+i_{osc}$	*0*	i_{MPP}	0.4	0.9
Case 14	19--20	t_{15}-t_{16}	<P_L	*off*	0	0.2	0.6	i_{avg}	i_{osc}	*0*	i_{MPP}	0.4	0.9
Case 4	20-21		<P_L	*on*	1	0.6	0.7	*0*	i_{osc}	*CCM*	i_{MPP}	0.5	0.9
Case 15	21--23		>P_L	*on*	1	0.6	0.7	*0*	$i_{SCrat}+i_{osc}$	*CCM*	i_{MPP}	0.25	0.5
Case 16	23--24	t_{17}-t_{18}	>P_L	*on*	1	0.6	0.95	*0*	i_{osc}	*CCM*	i_{MPP}	0.25	0.5
Case 17	24--25	t_{16}-t_{17}	>P_L	*on*	1	0.4	0.7	i_{avg}	$i_{SCrat}+i_{osc}$	*CCM*	i_{MPP}	0.25	0.5
Case 18	25--26		>P_L	*on*	1	0.4	0.95	i_{avg}	i_{osc}	*CCM*	i_{MPP}	0.25	0.5
Case 19	26--28		>P_L	*on*	0	0.7	0.7	i_{avg}	$i_{SCrat}+i_{osc}$	*CCM*	i_{MPP}	0.25	0.9
Case 20	28--29	t_{18}-t_{19}	>P_L	*on*	0	0.7	0.95	i_{avg}	i_{osc}	*CCM*	i_{MPP}	0.25	0.9
Case 21	29--31		>P_L	*on*	0	0.95	0.7	*0*	$i_{SCrat}+i_{osc}$	*CCM*	i_{MPP}	0.25	0.9
Case 22	31--32	t_{19}-t_{20}	>P_L	*on*	0	0.95	0.95	*0*	i_{osc}	*CCM*	i_{MPP}	0.25	0.9
Case 23	32--34		>P_L	*off*	0	0.7	0.7	i_{avg}	$i_{SCrat}+i_{osc}$	*VCM*	i_{MPP}	0.25	0.9
Case 24	34--35	t_{21}-t_{22}	>P_L	*off*	0	0.7	0.95	i_{avg}	i_{osc}	*VCM*	i_{MPP}	0.25	0.9
Case 25	35--36		>P_L	*off*	0	0.45	0.7	i_{avg}	$i_{SCrat}+i_{osc}$	*0*	i_{MPP}	0.25	0.9
Case 26	36--37	t_{20}-t_{21}	>P_L	*off*	0	0.45	0.95	i_{avg}	i_{osc}	*0*	i_{MPP}	0.25	0.9
Case 27	37--38		>P_L	*off*	0	0.95	0.7	*0*	$i_{SCrat}+i_{osc}$	*VCM*	*VCM*	0.25	0.9
Case 28	38--40	t_{22}-t_{25}	>P_L	*off*	0	0.95	0.95	*0*	i_{osc}	*VCM*	*VCM*	0.25	0.9
dclc		t_{23}-t_{24}	>P_L	*off*	0	0.95	0.95	*0*	i_{osc}	*VCM*	*VCM*	0.25	0.9
aclc	38.25--40	t_{24}-t_{25}	>P_L	*off*	0	0.95	0.95	*0*	i_{osc}	*VCM*	*VCM*	0.25	0.9

DPM AC load shedding | Grid injecting | Grid mode transfer | dclc-DC load change

EPM AC and DC load shedding | *Off-MPPT operation of PV* | aclc-AC load change

and both B_L, S_L are updated to 0.5. From Fig. 9(c)–(d), it can be observed that at t = 1 s, the battery and supercapacitor keep on charging until the SoCs of the battery/supercapacitor reaches the new limit of 0.5. This eliminates the critical oscillation of HESS powers at SoC limits.

2) D-Off Peak Pricing Mode (Cases: 5–8): At t = 6 s, peak pricing is disabled and battery is allowed to charge up to the full capacity from grid. In Case 5, t = 6–8 s, SoC_B, and SoC_{SC} are set lower than B_U and S_U, respectively. This makes the battery and supercapacitor to charge with rated current until their SoCs reach the upper limit B_U and S_U, respectively. Similarly, Cases 6–8 can be observed from t = 8–12 s in Fig. 9 and Table II.

3) D-Islanded Mode (Cases: 9–14): At t = 12 s, the grid goes OFF. Therefore, the system enters into islanded mode, as shown in Fig. 9(e). In Cases 9 and 10, battery supplies the deficit power and inverter is operated in VCM to supply power to ac loads. For Cases 11 and 12, SoC_B is less than 0.5. Therefore, ac loads are shed by resetting the inverter pulses and battery supplies/absorbs deficit/excess power. For Cases 13 and 14,

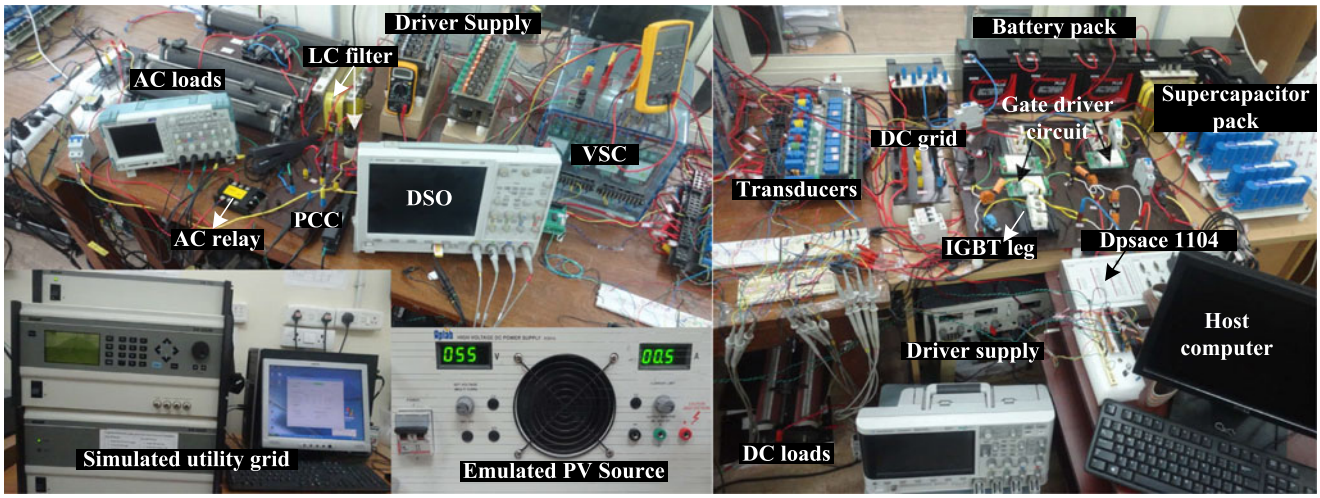

Fig. 10. Experimental setup of grid interactive microgrid with HESS.

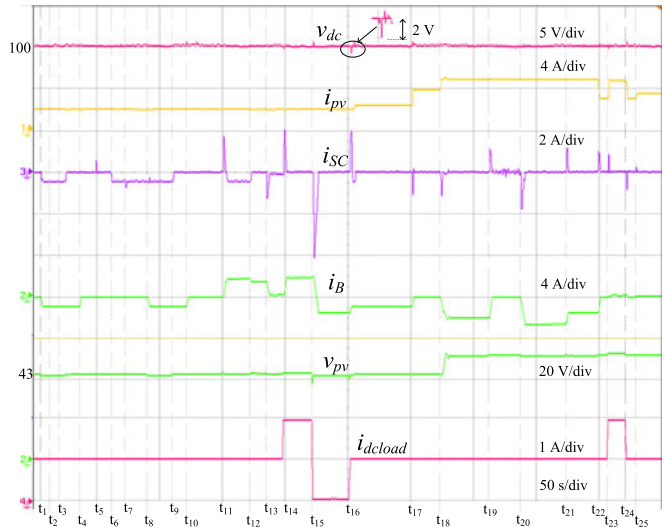

Fig. 11. Experimental results of proposed PMS: DC-link voltage, PV current, supercapacitor current, battery current, PV voltage, and dc load current.

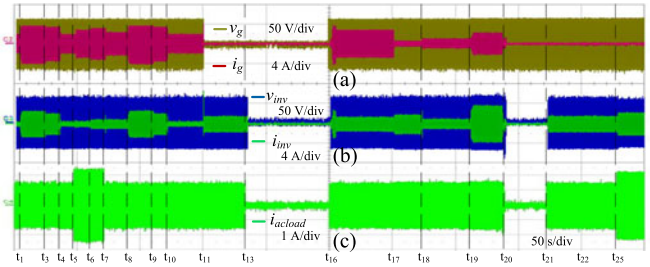

Fig. 12. Experimental results of proposed PMS. (a) Grid voltage and grid current. (b) Inverter voltage and inverter current. (c) AC load current.

SoC_B is made less than B_L and PV power is very low and not enough to supply loads. Therefore, both ac and dc loads are shed by PMA, as shown in Fig. 9(g)–(h), and battery is charged.

B. Excess Power Mode (Cases: 15–28)

E-peak pricing mode, i.e., Cases 15–18 and E-off peak pricing mode, i.e., Cases 19–22 are illustrated in Fig. 9 and given in Table II. At t = 21 s, i_{MPP} is increased from 4 to 6 A, as shown in Fig. 9(b), which makes the system to enter into grid injecting mode. Cases 23–26 are verified and tabulated in Table II. In E-islanded mode, at t = 32 s the grid goes OFF, i.e., the system enters into islanded mode and the corresponding Cases 23–26 are tabulated in Table II. At t = 37 s, both SoC_B and SoC_{SC} are set higher than their upper limits B_U and S_U, respectively. As the system is in islanded mode and HESS is fully charged, PV is operated in *off-MPPT mode* till t = 38.5 s, as shown in Fig. 9(b). *Off-MPPT* is achieved by changing PV reference current i_{PVref} from i_{MPP} to i_{avg}.

V. Experimental Results

The experimental setup of hybrid microgrid with HESS is shown in Fig. 10. It consists of an emulated PV source, simulated utility grid, battery unit, supercapacitor unit, HGBC, two bidirectional converters, dc and ac loads, and a single-phase VSC. The proposed PMS is implemented in real time using dSPACE 1104 control board.

The parameters used for experimental study are given in Table I. There are 28 cases grouped into six modes, as shown in Fig. 2. Only 18 cases are shown in the experimental results and rest ten cases are omitted. Because, in those cases, only the supercapacitor goes into charging mode and rest of the system operation remains same as its preceding or following case.

The PMS is initiated at t_1 instant with battery and supercapacitor SoCs less than their lower limits of 0.25 and 0.2, respectively. Therefore, both battery and supercapacitor charge from grid, as shown in Fig. 11, until their SoCs reach the updated lower limit of 0.5. Similarly, all operating modes are illustrated in Fig. 11 and tabulated in Table II. Few important modes are discussed in the following section.

In Mode C, i.e., deficit islanded mode, at t_{11} instant, the grid voltage is decreased to zero, as shown in Figs. 12 and 13(a).

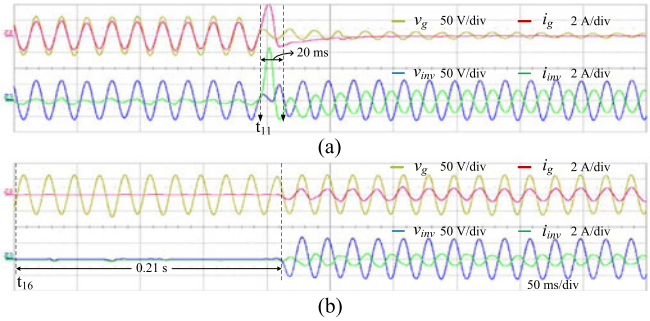

Fig. 13. Experimental results showing islanding and resynchronization. (a) Zoomed view of Fig. 12 at t_{11} instant. (b) Zoomed view of Fig. 12 at t_{16} instant.

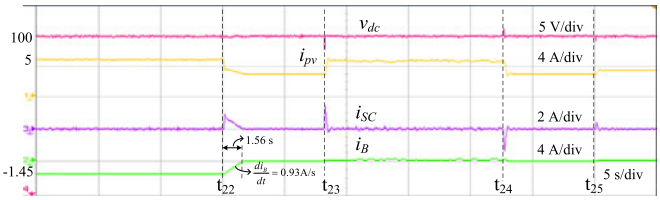

Fig. 14. Experimental results showing *off-MPP* operation. Zoomed view of $v_{\rm dc}$, i_{pv}, $i_{\rm SC}$, and i_B from Fig. 11.

The PMA detects the disturbance and islands the microgrid by activating the grid relay. As the $\rm SoC_B$ is more than 0.5, ac loads are supplied power by restoring voltage on ac side of VSC, as shown in Fig. 13(a). The islanding of microgrid is achieved in 20 ms, which can be observed from Fig. 13(a). This value satisfies the requirement of 0.16 s given in the IEEE Standard 1547. At t_{16} instant, the utility grid voltage is restored. The PMA detects the grid voltage restoration and closes the relay in 0.21 s, as shown in Fig. 13(b). It can be noticed that the ac loads are OFF from $t_{13} - t_{16}$, as $\rm SoC_B$ is less than 0.5 in islanded mode.

In Mode F, i.e., excess islanded mode, at t_{22} instant both $\rm SoC_B$ and $\rm SoC_{SC}$ are set to 0.95, which is higher than their upper limits (0.9) and $i_{\rm MPP}$ is increased to 6 A. This forces the system to operate in *off-MPPT mode* and $i_{\rm pv}$ decreases to 3 A, as illustrated in Fig. 14. It can be noticed that the dc load is increased by 100% at t_{23} instant, due to which $i_{\rm pv}$ increases from 3 to 5 A, as shown in Fig. 14. At t_{23} instant the dc load is decreased to 50%, due to which $i_{\rm pv}$ decreases from 5 to 3 A, as shown in Fig. 14.

It can be noticed that due to battery current smoothing, the rate of change of battery current and peak overshoot of $v_{\rm dc}$ are decreased to 0.93 A/s and 2 V, respectively, compared to that of 1.8 A/s and 5.2 V in [8].

In grid-connected mode, at t_{26} instant the PV current is increased from 0.5 to 4.5 A, as shown in Fig. 15(a), by keeping $\rm SoC_B$ and $\rm SoC_{SC}$ higher than their upper limits. This forces the system to enter into excess power mode. As battery and supercapacitor are fully charged, the excess power is injected into the grid, as shown in Fig. 15(a). The sudden increase in PV power is absorbed by supercapacitor and the grid current

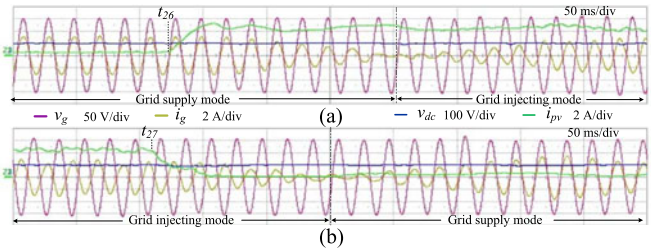

Fig. 15. Experimental results showing seamless mode transfer of grid: $v_{\rm dc}$, i_{pv}, v_g, and i_g during (a) mode transfer from grid supply mode to grid injecting mode and (b) mode transfer from grid injecting mode to grid supply mode.

TABLE III
PERFORMANCE COMPARISON BETWEEN VARIOUS PMSS

Parameters	Scheme I	Scheme II	Proposed PMS
DC-link voltage ($v_{\rm dc}$)			
$t_s\,(s)$	0.15	0.25	0.2
$Mp(\%)$	10	5.3	2
e_{ss} (V)	4	0.1	0.1
Battery current di_B/dt	25 A/s	1.4 A/s	0.93 A/s
%THD	5.2%	4.2%	3.6%

i_g changes from 3 A in phase with grid voltage v_g to 0 A and increases to 3 A in out of phase with grid voltage v_g in 0.35 s, as shown in Fig. 15(a). This seamless phase reversal of i_g eliminates the oscillations during mode transfer of the grid.

Similarly, mode transfer from grid injecting mode to grid supply mode is illustrated in Fig. 15(b). It can also be noticed that i_g is sinusoidal and in phase with v_g in grid supply mode and in exactly out of phase with v_g in grid injecting mode and the total harmonic distortion (THD) of i_g is found to be 3.6%, which illustrates the power quality features of proposed PMS.

In this table, t_s, Mp, $e_{\rm ss}$, and di_B/dt represent settling time, peak overshoot, steady state error of $v_{\rm dc}$ and rate of change of battery current, respectively.

The performance of proposed PMS is compared with PMS given in [10] (scheme I) and [8] (scheme II) and key observations are given in Table III. The proposed method has superior performance compared to scheme-I and scheme-II.

VI. CONCLUSION

A unified power management scheme was proposed for a grid interactive hybrid microgrid with HESS. The new method of identifying microgrid operating mode was proposed and verified in all possible operating modes. The formulated PMS addresses the possible operating modes of the microgrid and achieves stable and desirable performance. It was shown that the proposed PMS ensures reliable and continuous power supply to the local loads and enables the bidirectional real power transfer between the microgrid and the utility grid while improving the power quality aspects at the PCC. Various features like fast dc-link voltage regulation, reduced battery current stresses, *Off-MPPT* operation were illustrated. The proposed PMS achieves seamless mode transfer using supercapacitor units. The power quality at the point of common coupling was maintained as per the grid

standards. Also, the proposed PMS does not require forecasting of weather and measurement load currents/powers, which reduces the complexity and number of sensors.

REFERENCES

[1] O. Lucia, I. Cvetkovic, H. Sarnago, D. Boroyevich, P. Mattavelli, and F. Lee, "Design of home appliances for a dc-based nanogrid system: An induction range study case," *IEEE J. Emerg. Sel. Topics Power Electron.*, vol. 1, no. 4, pp. 315–326, Dec. 2013.

[2] F. Nejabatkhah and Y. W. Li, "Overview of power management strategies of hybrid ac/dc microgrid," *IEEE Trans. Power Electron.*, vol. 30, no. 12, pp. 7072–7089, Dec. 2015.

[3] P. Denholm *et al.*, "Bright future: Solar power as a major contributor to the U.S. grid," *IEEE Power Energy Mag.*, vol. 11, no. 2, pp. 22–32, Mar. 2013.

[4] S.-T. Kim, S. Bae, Y. C. Kang, and J.-W. Park, "Energy management based on the photovoltaic HPCS with an energy storage device," *IEEE Trans. Ind. Electron.*, vol. 62, no. 7, pp. 4608–4617, Jul. 2015.

[5] R. Dougal, S. Liu, and R. White, "Power and life extension of battery-ultracapacitor hybrids," *IEEE Trans. Compon. Packag. Technol.*, vol. 25, no. 1, pp. 120–131, Mar. 2002.

[6] C. Abbey and G. Joos, "Supercapacitor energy storage for wind energy applications," *IEEE Trans. Ind. Appl.*, vol. 43, no. 3, pp. 769–776, May 2007.

[7] F. Baalbergen, P. Bauer, and J. Ferreira, "Energy storage and power management for typical 4Q-load," *IEEE Trans. Ind. Electron.*, vol. 56, no. 5, pp. 1485–1498, May 2009.

[8] N. R. Tummuru, M. K. Mishra, and S. Srinivas, "Dynamic energy management of renewable grid integrated hybrid energy storage system," *IEEE Trans. Ind. Electron.*, vol. 62, no. 12, pp. 7728–7737, Dec. 2015.

[9] G. Wang, M. Ciobotaru, and V. Agelidis, "Power smoothing of large solar PV plant using hybrid energy storage," *IEEE Trans. Sustain. Energy*, vol. 5, no. 3, pp. 834–842, Jul. 2014.

[10] B. I. Rani, G. S. Ilango, and C. Nagamani, "Control strategy for power flow management in a PV system supplying dc loads," *IEEE Trans. Ind. Electron.*, vol. 60, no. 8, pp. 3185–3194, Aug. 2013.

[11] Y.-M. Chen, H.-C. Wu, Y.-C. Chen, K.-Y. Lee, and S.-S. Shyu, "The ac line current regulation strategy for the grid-connected PV system," *IEEE Trans. Power Electron.*, vol. 25, no. 1, pp. 209–218, Jan. 2010.

[12] F. Savoye, P. Venet, M. Millet, and J. Groot, "Impact of periodic current pulses on Li-ion battery performance," *IEEE Trans. Ind. Electron.*, vol. 59, no. 9, pp. 3481–3488, Sep. 2012.

[13] L. Chen and S. Mei, "An integrated control and protection system for photovoltaic microgrids," *CSEE J. Power Energy Syst.*, vol. 1, no. 1, pp. 36–42, Mar. 2015.

[14] D. Wang and F. Z. Peng, "Smart gateway grid: A dg-based residential electric power supply system," *IEEE Trans. Smart Grid*, vol. 3, no. 4, pp. 2232–2239, Dec. 2012.

[15] M. Sechilariu, B. Wang, and F. Locment, "Building integrated photovoltaic system with energy storage and smart grid communication," *IEEE Trans. Ind. Electron.*, vol. 60, no. 4, pp. 1607–1618, Apr. 2013.

[16] S. Lee, G. Son, and J.-W. Park, "Power management and control for grid-connected DGs with intentional islanding operation of inverter," *IEEE Trans. Power Syst.*, vol. 28, no. 2, pp. 1235–1244, May 2013.

[17] M. Hosseinzadeh and F. Salmasi, "Power management of an isolated hybrid ac/dc micro-grid with fuzzy control of battery banks," *IET Renew. Power Gener.*, vol. 9, no. 5, pp. 484–493, 2015.

[18] Y. K. Chen, Y. C. Wu, C. C. Song, and Y. S. Chen, "Design and implementation of energy management system with fuzzy control for dc microgrid systems," *IEEE Trans. Power Electron.*, vol. 28, no. 4, pp. 1563–1570, Apr. 2013.

[19] S. Teleke, M. Baran, S. Bhattacharya, and A. Huang, "Rule-based control of battery energy storage for dispatching intermittent renewable sources," *IEEE Trans. Sustain. Energy.*, vol. 1, no. 3, pp. 117–124, Oct. 2010.

[20] H. Kanchev, D. Lu, F. Colas, V. Lazarov, and B. Francois, "Energy management and operational planning of a microgrid with a PV-based active generator for smart grid applications," *IEEE Trans. Ind. Electron.*, vol. 58, no. 10, pp. 4583–4592, Oct. 2011.

[21] H. Fakham, D. Lu, and B. Francois, "Power control design of a battery charger in a hybrid active PV generator for load-following applications," *IEEE Trans. Ind. Electron.*, vol. 58, no. 1, pp. 85–94, Jan. 2011.

[22] C. Jin, P. Wang, J. Xiao, Y. Tang, and F. H. Choo, "Implementation of hierarchical control in dc microgrids," *IEEE Trans. Ind. Electron.*, vol. 61, no. 8, pp. 4032–4042, Aug. 2014.

[23] D. Chen, L. Xu, and L. Yao, "Dc voltage variation based autonomous control of dc microgrids," *IEEE Trans. Power Del.*, vol. 28, no. 2, pp. 637–648, Apr. 2013.

[24] B. Hredzak, V. Agelidis, and G. Demetriades, "A low complexity control system for a hybrid dc power source based on ultracapacitor-acid battery configuration," *IEEE Trans. Power Electron.*, vol. 29, no. 6, pp. 2882–2891, Jun. 2014.

[25] S. I. Ganesan, D. Pattabiraman, R. K. Govindarajan, M. Rajan, and C. Nagamani, "Control scheme for a bidirectional converter in a self-sustaining low-voltage dc nanogrid," *IEEE Trans. Ind. Electron.*, vol. 62, no. 10, pp. 6317–6326, Oct. 2015.

[26] B. Hredzak, V. Agelidis, and M. Jang, "A model predictive control system for a hybrid battery-ultracapacitor power source," *IEEE Trans. Power Electron.*, vol. 29, no. 3, pp. 1469–1479, Mar. 2014.

[27] H. Liu, Z. Zabinsky, and W. Kohn, "Rule-based control system design for smart grids," in *Proc. IEEE Power Energy Soc. Gen. Meeting*, Jul. 2010, pp. 1–5.

[28] H. Zeineldin and J. Kirtley, "A simple technique for islanding detection with negligible nondetection zone," *IEEE Trans. Power Del.*, vol. 24, no. 2, pp. 779–786, Apr. 2009.

Srikanth Kotra (SM'15) was born in Lingala, India, in 1991. He received the Bachelor's degree from Jawaharlal Nehru Technological University, Hyderabad, India, in 2012. He is currently working toward the Ph.D. at the Indian Institute of Technology Madras, Chennai, India.

His research interests include power electronic converter applications in microgrid and renewable energy systems and electric vehicles.

Mr. Kotra received the Best Paper Award at the 2015 IEEE India Conference, New Delhi, India, and the Best Presentation Award at the 2015 IEEE Industrial Electronics Conference, Yokohama, Japan.

Mahesh Kumar Mishra (S'00–M'02–SM'10) received the B.Tech. degree from the College of Technology, Pantnagar, India, in 1991, the M.E. degree from the University of Roorkee, Roorkee, India, in 1993, and the Ph.D. degree in electrical engineering from the Indian Institute of Technology, Kanpur, India, in 2002.

He has about 25 years of teaching and research experience. For about ten years, he was with the Department of Electrical Engineering, Visvesvaraya National Institute of Technology, Nagpur, India. He is currently a Professor in the Department of Electrical Engineering, Indian Institute of Technology Madras, Chennai, India. His interests are in the areas of power distribution systems, power electronic applications in microgrid, and renewable energy systems.

Prof. Mahesh is a Life Member of the Indian Society of Technical Education.